Numerical Simulation of a Flexible X-Wing Flapping-Wing Micro Air Vehicle

Deng, Shuanghou; Perçin, Mustafa; van Oudheusden, Bas; Bijl, Hester; Remes, Bart; Xiao, T

DOI
10.2514/1.J054816

Publication date
2017

Document Version
Accepted author manuscript

Published in
AIAA Journal: devoted to aerospace research and development

Citation (APA)
Deng, S., Perçin, M., van Oudheusden, B., Bijl, H., Remes, B., & Xiao, T. (2017). Numerical Simulation of a Flexible X-Wing Flapping-Wing Micro Air Vehicle. *AIAA Journal: devoted to aerospace research and development*, *55*(7), 2295-2306. https://doi.org/10.2514/1.J054816

Popstprint of AIAA Journal, Vol. 55, No. 7 (2017), pp. 2295-2306.
https://doi.org/10.2514/1.J054816

AIAA

Numerical Simulation of a Flexible X-wing Flapping Wing Micro-Air-Vehicle

S. Deng[1], M. Percin[3], B.W. van Oudheusden[4], H. Bijl[5] and B. Remes[6]
Delft University of Technology, Delft, the Netherlands, 2629 HS
nd
T. Xiao[2]
Nanjing University of Aeronautics and Astronautics, Nanjing, China, 210016

Numerical simulations were performed to investigate the flow field around a flexible flapping-wing micro air vehicle (MAV) using an in-house developed CFD solver. To include the dynamics of the flexible wings and its impact on the aerodynamic behavior of the MAV, the wing deformation pattern during flapping was experimentally determined by a stereo-vision measurement. This data was subsequently interpolated to be employed as prescribed flapping kinematics in the numerical flow simulations, using a CFD solver that is based on a deformable overset grid method. The computational results of the hovering configuration provide a quantitative prediction of the unsteady aerodynamics of the flapping-wing MAV in terms of aerodynamic force production and flow structures. The formation and evolution of the leading/trailing edge vortex and tip vortex were visualized. Additionally, by introducing an incoming freestream flow velocity in the simulations, the flow structure related to the forward flight configuration is investigated. The forces and the flow structures are compared with the experimental results from force and DPIV measurements; a good agreement was illustrated that further evidenced the capability of the numerical methodology proposed in the present study.

[1] Ph.D researcher, Faculty of Aerospace Engineering, Kluyverweg 1, s.deng@nwpu.edu.cn, AIAA student member.
[2] Associate professor, College of Aerospace Engineering, Yudao Street 29, xthang@nuaa.edu.cn.
[3] Ph.D researcher, Faculty of Aerospace Engineering, Kluyverweg 1, m.percin@tudelft.nl,AIAA student member.
[4] Associate professor, Faculty of Aerospace Engineering, Kluyverweg 1, b.w.vanoudheusden@tudelft.nl .
[5] Full professor, Faculty of Aerospace Engineering, Kluyverweg 1, h.bijl@tudelft.nl.
[6] Project manager, Faculty of Aerospace Engineering, Kluyverweg 1, b.d.w.remes.@tudelft.nl.

Nomenclature

C_d = drag coefficient

$\overline{C_d}$ = period-averaged drag coefficient

C_l = lift coefficient

$\overline{C_l}$ = period-averaged lift coefficient

C_T = thrust coefficient

C_P = pressure coefficient

c = chord, mm

d = diameter, mm

f = flapping frequency, Hz

H = plunging amplitude

k = reduced frequency

Ma = Mach number

Re = Reynolds number

T = period time, s

t = physical time, s

U_∞ = freestream velocity, m/s

Φ = flapping phase angle, deg

ω = vorticity, s^{-1}

Subscript

$_{in}$ = instroke

$_{out}$ = outstroke

I. Introduction

Micro air vehicles (MAVs) have been defined as flying vehicles with proposed geometric dimensions less than 15 cm in every direction and a weight less than 100 gram [1]. MAVs have attracted more attention recently due to their potential in civilian and military application. Existing MAVs can be categorized into three concepts, *viz.*, fixed wing, rotary wing and flapping wing MAVs. The flapping-wing MAVs, often inspired by biological flyers, have attracted considerable attention in view of their excellent maneuverability and flight capabilities at the low Reynolds number (typically $10^3 \sim 10^5$) regime. Like natural flyers, flapping-wing MAVs are usually equipped with a single or multiple pair of flexible wings that generate both thrust and lift at the same time. Compared to more conventional rotary propelling concepts, flapping motion benefits from a number of unsteady aerodynamic effects such as the clap-and-fling (or Weis-Fogh [2]) mechanism, delayed stall [3] and wake capture [4]. Exploiting the knowledge obtained in the area of flapping-wing aerodynamics, the design and development of flapping-wing MAVs has advanced since the 1990s. The MicroBat [5] developed by AeroVironment and Caltech, Inc., under the Defense Advanced Research Projects Agency (DAPAR) funding support, was the first palm-size flapping wing MAV, which has three-channel radio control and was powered by a light lithium-polymer battery. Later on, in 2011 they developed a flapping-wing MAV prototype, namely the "Nano Hummingbird" (http://www.avinc.com/nano), which was a huge breakthrough in flapping-wing MAV research because of it gyroscopically stabilized flight without any tail control surfaces. Recently, the Harvard University used Micro-Electro-Mechanical System (MEMS) techniques [6] to develop the world smallest ornithopter with a total length of 3 cm, which currently allows maneuvering flight with an external wire connected power supply. To obtain a better understanding with respect to the flapping locomotion in nature and apply the state-of-art knowledge on the flapping robots, the MAV laboratory in the Delft University of Technology has developed a small-scale ornithopter, namely the DelFly [7], which is equipped with an X-wing configuration with two pairs of wings. The wings exhibit a clap-and-fling motion during the flapping cycle on both sides of the fuselage. The particular motivation for this configuration is that it can generate more lift during flight and provide a stable flight by minimizing rocking amplitude, and hence making- the DelFly an ideal stable platform for onboard cameras. Substantial experimental studies have been performed on the DelFly MAVs, including the DelFly II and the DelFly Micro, the latter being the smallest (total wing span: 10 cm; mass: 3 gram) member in the DelFly family. The force generation and the flow topology of the DelFly configuration have been experimentally addressed via force balance and Particle Image Velocimetry (PIV) measurements. Percin et al. [8] experimentally investigated the

formation and evolution of the unsteady three-dimensional wake structures generated by the DelFly II flapping-wing MAV in a forward flight configuration, using time-resolved stereoscopic particle image velocimetry (Stereo-PIV) measurement. Tenaglia et al. [9] subsequently conducted a Stereo-PIV in combination with force measurement on the DelFly II in hovering flight configuration. The vortex formation around the wing was investigated by orienting the laser measurement sheet at different spanwise locations; however, it remains difficult to obtain an accurate representation of the three-dimensional vortex structure in the vicinity of the wing. Alternatively, numerical simulation may be a suitable approach to obtain a full three-dimensional flow topology around the flexible flapping-wing MAVs in both near and far-field. Until now, some numerical studies have been done related to the DelFly flapping-wing MAV. The first numerical investigation related to DelFly is documented by Gillebaart et al. [10], who studied the influence of wing flexibility and the clap-and-peel motion on the thrust generation in hover conditions using two-dimensional CFD simulations. The wing deformations derived from PIV measurements [11] were used in their study to simulate the flexibility of the wing. Later, Tay et al. [12] used an Immersed Boundary Method (IBM) to investigate the aerodynamic performance by varying kinematic and morphological parameters. However, using a prescribed user-defined motion has its limitations in accurately predicting the real flow structure occurring around the DelFly.

In general, numerically simulating the DelFly II or indeed any other flexible flapping-wing MAV has two major challenges: (1) accurate prediction of the wing deformation; (2) dealing with the large displacement and relative motion of multiple bodies. The Fluid-Structure Interaction (FSI) modelling of the highly flexible membrane wings is challenging due to the extremely flexible membrane used on the wing. Moreover, the presence of the carbon stiffeners gives the flapping wing an anisotropic construction, which makes the FSI modelling even more difficult. As an alternative approach, the present study uses data of the actual morphological deformation during flapping obtained experimentally by means of a stereo-vision technique, as input to represent the aero-elastic effect in the numerical simulations. By doing so, the fluid to structure interaction is absent, which principally eliminates the necessity of employing a structural model of the complex three-dimensional wing. Regarding the flow simulation, with the DelFly displaying large flapping amplitudes and using a clap-and-fling mechanism to achieve stable flight, this configuration challenges the existing Arbitrary Lagrangian Eulerian (ALE) based dynamic mesh techniques, since the mesh between the wings will experience large displacement during the simulation which can easily result in grid crossings thus abort the solver. In view of this difficulty, we developed a deformable overset grid technique

to implement the flow simulation involving multiple bodies undergoing large displacement movement and deformation [13] which will be used in the present study.

This paper is organized as follows: in section II, the DelFly flapping-wing MAV, the wing deformation measurement and the computational methodology will be introduced. Subsequently, the in-house developed CFD solver will be validated in Section III. Section IV will present the results, while discussion and comparison with experimental results followed by a conclusion is contained in Section V.

II. Materials and Methods

A. The Flapping-Wing MAV 'DelFly'

In Figure 1, the DelFly flapping-wing MAV and its geometric details are shown. As shown in Figure 1(b), the DelFly wing has a half-span length of 140 mm while the mean chord length is around 80 mm. The flexible wing is built from 10 μm Mylar membrane by a semi-automatic manufacturing method [14]. The leading edge is strengthened with a carbon rod of semicircular shape (d = 1.4 mm), while the stiffeners (dashed lines in Figure 1(b)) on the wing are round carbon rods (d = 0.28 mm). The layout of the wing was experimentally optimized [15] in terms of thrust-to-power ratio which is an indicator for evaluating the propulsive efficiency. The wings are attached to a crank system which actuates the flapping motion, where the flapping amplitude is 44 deg for each wing. The dihedral angle is 12 deg as indicated in Figure 1(c). In the numerical simulation and stereo-vision measurement, the tail and the onboard electronic devices were removed for the sake of simplification. During the measurement, the flapping frequency was set at 8 Hz with a corresponding Reynolds number ($Re = U_{tip}c_m/\nu$, U_{tip} is the mean tip velocity, c_m is the mean chord length, and ν is the kinematic viscosity of the air) of about 20,000. The numerical simulations will be conducted using the same conditions as in the experiments.

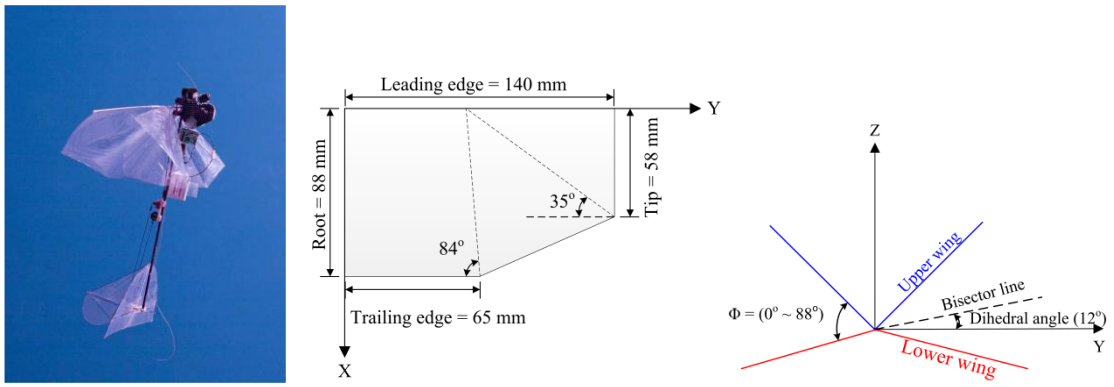

(a) (b) (c)

Figure 1 The DelFly flapping wing MAV and its geometric dimensions: (a) DelFly in hovering flight; (b) wing planform (only half wing is shown); (c) schematic front view of the flapping wing arrangement.

B. Wing Deformation Measurements

For reasons outlined in the introduction, the morphological model of the flexible DelFly wing has been constructed based on experimental deformation measurements. For this, markers on the wing (as shown in Figure 2(a)) were instantaneously traced via a stereo-vision system. The experimental setup is illustrated in Figure 2(b), where two high-speed cameras (Photron SA 1.1), indicated as Cam1 and Cam2, with a resolution of 1024×1024 pixels were used to record the wing markers with an azimuth angle at 45 deg. The wing was illuminated by a powerful spotlight from below, using a white paper sheet to create a diffusive white background so as to identify the markers on the wing. Note that a third camera (labelled as 'PosCam') in Figure 2(b) mounted in front of the DelFly was employed to capture the leading edge position during flapping to define the phase angle. Given a flapping frequency of the DelFly around 8 Hz, all the cameras were operated at a recording frequency of 1 kHz and 1000 images were taken to provide sufficient temporal resolution and for resolving the flapping cycle. The DelFly was mounted on a miniature load cell (ATI Nano-17), with which the temporal variation of the aerodynamic force (i.e. thrust) was instantaneously captured. The thrust variation with time was used to compare with the computed thrust to validate the numerical capability.

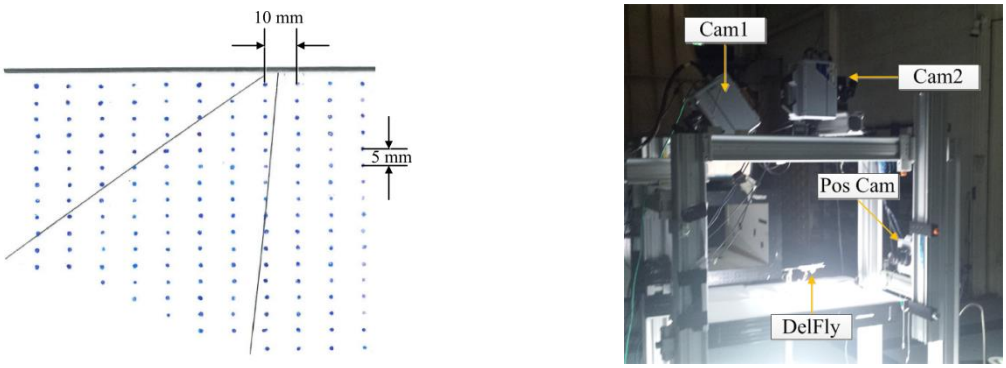

(a) (b)

Figure 2 Stereo vision deformation experiment; (a) markers on the wing; (b) setup.

The three-dimensional coordinates of the markers are reconstructed by a stereo triangulation technique [16]. The reconstruction of the markers on the wing at a certain time instant (t/T = 0.4) is illustrated in Figure 3(a). With respect to the spanwise dimension, the reconstruction was only performed from 3 cm from the root to the tip; the

very root part is omitted since it is not very influential on the flow field and is also not convenient for the numerical simulation. Note that there are in total 166 marker points on the wing, which is insufficient as an input for the CFD solver to fully reconstruct the deformation pattern. Moreover, the leading edge, tip and trailing edge of the wings are not reconstructed in the stereo-triangulation process while these regions are also important in predicting the aerodynamic performance. Therefore, the marker data is utilized to define the wing contour via an extrapolation. . Additionally, to obtain smooth and dense deformation data that can be conveniently used as input for the numerical simulation, a further interpolation of the experimental deformation data (Figure 3(a)) was performed using a Kriging regression technique [17], which can inherently process the unstructured scattered data. The raw deformation data was regressed on a structured mesh with size of 23×18, thus 414 points at each time step. Additionally, the Kriging regression technique also considers the triangulation displacement as an error input to instantaneously correct the wing surface where large disparity occurs. Figure 3(b) shows the interpolated deformation pattern in a structured mesh manner.

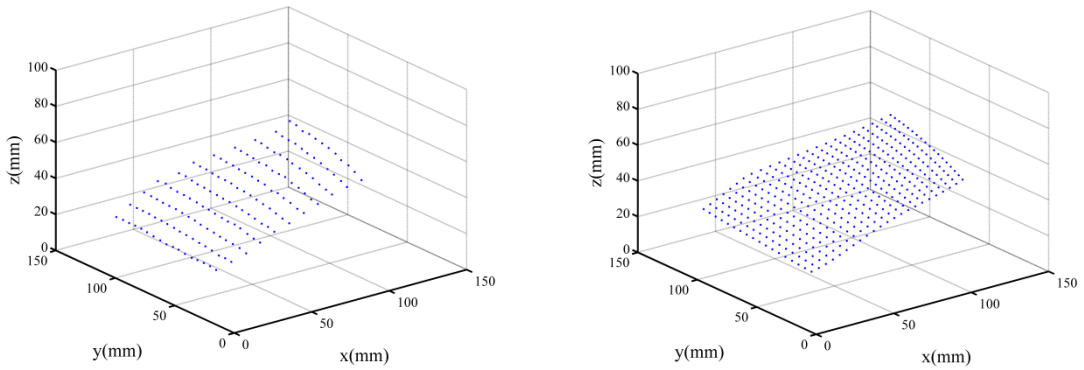

(a) (b)

Figure 3 Deformation pattern at t/T = 0.4: (a) raw data from stereo triangulation; (b) dense deformation data from Kriging interpolation.

Except for the spatial interpolation, the Kriging regression was also used to perform a temporal interpolation to obtain the deformation pattern at multiple time moments based on available data. To temporally resolve the flow structure development during the flapping motion, 100 equidistant time moments within one flap cycle were interpolated from 20 sets of the stereo-vision data. Figure 4 shows the wing deformation pattern with a 0.02c thickness at different instants during one flapping cycle. Note that for the sake of clear visualization, the deformation data is only shown subsampled to an increment of 10 time steps. The assumption was made that the upper and lower wings have similar deformation patterns, since the DelFly uses a symmetric driving system. Therefore, the

measurement was only performed on the upper wing, while the deformation of the lower wing is obtained by mirroring the upper wing deformation with respect to the dihedral plane.

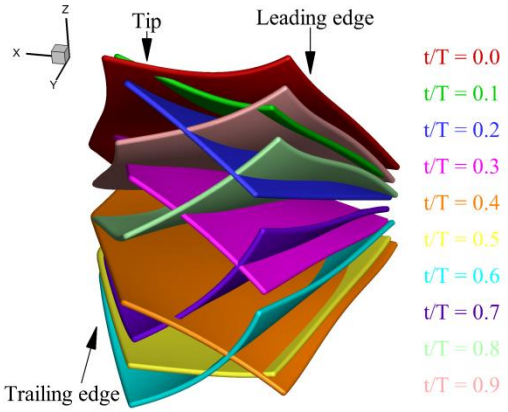

Figure 4 Deformation of the DelFly wing during one flapping cycle.

C. Numerical Methodology and Setup

The Preconditioning Governing Equation

The unsteady viscous flow generated by the DelFly flapping-wing MAV is numerically simulated by an in-house developed CFD solver. The code solves the compressible flow equations by a Finite Volume Method (FVM), and a low Mach number preconditioning technique is applied to extend its application in the low speed flow region. Preconditioning [18,19,20] is needed for low speed flow because compressible flow algorithms tend to perform poorly for flows in the incompressible limit in terms of convergence, stability and accuracy, predominately due to the large disparity between the acoustic and convective wave speeds. Low Mach number preconditioning modifies the governing equations without altering the steady-state solution, in such way that their eigenvalues are all of the same order, allowing for an efficient and accurate solution at low Mach numbers. The advantage of preconditioning is that it enables a solution method applicable at all Mach numbers. In order to obtain meaningful solutions for unsteady flow, it is necessary to use a dual-time stepping approach in which a pseudo time is introduced to advance the solution at each physical time level. The governing equations with a preconditioned pseudo-time derivative term can be formulated as

$$\mathbf{\Gamma}\frac{\partial}{\partial \tau}\int_{\Omega(t)}\mathbf{Q}\,\mathrm{d}V+\frac{\partial}{\partial t}\int_{\Omega(t)}\mathbf{W}\,\mathrm{d}V+\oint_{S(t)}(\mathbf{F}(\mathbf{W})-v_g\mathbf{W})\,\mathrm{d}S=\oint_{S(t)}\mathbf{F}_v\,\mathrm{d}S \tag{1}$$

where, τ and *t* are the pseudo and physical time, respectively. The conservative variables $\mathbf{W} = (\rho, \rho u, \rho v, \rho w, \rho e)^{T}$ and the primitive variable vector $\mathbf{Q} = (p, u, v, w, T)^{T}$, while $\mathbf{F}(\mathbf{W})$ and $\mathbf{F}_v$ are the convective and viscous fluxes, respectively; v_g is the contra-variant velocity of the boundary $S(t)$ of the control volume Ω(t). The preconditioning matrix $\mathbf{\Gamma}$ is given as below

$$\mathbf{\Gamma} = \begin{bmatrix} \rho_p^{'} & 0 & 0 & 0 & \rho_T \\ u\rho_p^{'} & \rho & 0 & 0 & u\rho_T \\ v\rho_p^{'} & \rho & 0 & 0 & v\rho_T \\ w\rho_p^{'} & \rho & 0 & 0 & w\rho_T \\ \rho_P^{'} H_0 & \rho u & \rho v & \rho w & \rho_T h_0 + \rho h_T \end{bmatrix} \tag{2}$$

where $\rho_p^{'} = \dfrac{1}{\beta^{'} \alpha^2}$ *and* $\beta^{'} = \dfrac{1}{1+(\gamma-1)\beta}$*; a is* the speed of sound and β is the preconditioning parameter, defined as

$$\beta = \min(\max(Ma_{\max}^2, \beta_{\min}), 1.0) \tag{3}$$

For flow fields which involve moving boundaries, the maximal local Mach number is formulated as

$$Ma_{\max} = \max\left(\frac{\left|\vec{V} - \vec{V_g}\right|_{cell}}{\alpha}, \frac{\left|\vec{V} - \vec{V_g}\right|_{neighbors}}{\alpha}\right) \tag{4}$$

here, $\vec{V}$ and $\vec{V_g}$ are the flow and grid velocity, respectively, while the subscript *cell* and *neighbors* refer to current control volume and its adjacent volumes. In the present study, we define

$$\beta_{\min} = 3\max(Ma_{\infty}^2, Ma_{g,mean}^2) \tag{5}$$

where Ma_{∞} and $Ma_{g,mean}$ are the inflow Mach number and the mean Mach numbers of moving objects, respectively. Note that, when $Ma_{\infty} \rightarrow 1$ or $Ma_{g,mean} \rightarrow 1$, the preconditioned equation will be degraded into a non-preconditioned one. The governing equations are discretized using a second-order upwind cell-centred scheme in space and solved by an implicit iteration on hybrid unstructured meshes. The FGMRES (Flexible generalized minimal residual method) [21] method is applied to solve the linear equations in the governing equation. In view of the complexity of flapping wing locomotion in this study, a steady computation will be firstly run without flapping the wings. The resulting steady solution will be used as the initial flow condition for the transient computation. A convergence criteria is determined (residuals down to 10^{-3}) for the sake of terminating the computation. More details of the CFD solver can be found in Ref [13].

Boundary Conditions

Introducing the preconditioning equation can definitely change the original governing equations in term of eigenvalues and eigenvectors. It is therefore the far-field, locally one-dimensional characteristic boundary conditions are developed in this manuscript were developed for the sake of adjusting the preconditioned equations. By considering the linearized inviscid preconditioned equations

$$\frac{\partial \mathrm{Q}}{\partial t} + \Gamma^{-1} A_{\Gamma} \frac{\partial Q}{\partial t} = \frac{\partial Q}{\partial t} + X \Lambda X^{-1} \frac{\partial Q}{\partial t} = 0 \tag{6}$$

Eqn. 6 then can be diagonalized using a similarity transformation to yield a decoupled system of equations. $(dw/dt) + \Lambda(dw/dx) = 0$, where w represents the vector of the characteristic variables. The X^{-1} is

$$X^{-1} = \begin{bmatrix} -(\gamma - 1)/\gamma R\rho & 0 & 1 \\ 1 & A & 0 \\ 1 & B & 0 \end{bmatrix} \tag{7}$$

where $A = \rho(\lambda_4 - \beta\theta)$, $B = \rho(\lambda_5 - \beta\theta)$. The *w* can be then formulated as

$$w = \begin{bmatrix} w_1 \\ w_2 \\ w_3 \end{bmatrix} = \begin{bmatrix} -(\gamma - 1)\, p/\gamma R\rho_0 \\ p + A_0\theta \\ p + B_0\theta \end{bmatrix} \tag{8}$$

One assumption has to be made that the directions of the normal vector on the boundaries are pointing outward. For subsonic flowfield, the second eigenvalue $1/2(\beta+1)(\theta - V_g) + 1/2\sigma$ is always positive, w_2 on the boundary is identical as in the interior of the mesh. Similarly, the third eigenvalue $1/2(\beta+1)(\theta - V_g) - 1/2\sigma$ is always negative and thus the w_3 on the boundary is the same as in the free stream. The relationship between the values of w_1 on the boundary depends on whether or not the flow is into or out of the domain, for inflow, the $\theta - V_g < 0$, the value on the boundary is the same as in the free stream, alternatively, for outflow, $\theta - V_g \geq 0$, it is the same as in the interior field.

The above mentioned provide three equations to solve the pressure, the normal velocity and the temperature on the far-field boundary:

$$\begin{bmatrix} -(\gamma-1)/\gamma R\rho_0 & 0 & 1 \\ 1 & A_0 & 0 \\ 1 & B_0 & 0 \end{bmatrix} \begin{bmatrix} p \\ \theta \\ T \end{bmatrix} = \begin{bmatrix} -(\gamma-1)p_r/\gamma R\rho_0 + T_r \\ p_{in} + A_0\theta_{in} \\ p_\infty + B_0\theta_\infty \end{bmatrix} \tag{9}$$

where the subscript *r* on the right-hand side of Eqn. 9 refers to the information extracted from outside of the domain for inflow and from inside of the domain for outflow. The subscript *in* indicates the information taken from inside of the domain and ∞ dipictes the information involved outside of the domain. Moreover, the boundary conditions for the solid wall and symmetry plane are treated following the implementation from Zhang and Wang [22].

Dynamic mesh strategy

In order to implement the motion of the wings instantaneously, a deformable overset grid method [13] based on RBF (Radial Basis Function)-based mapping is developed and coupled with the current CFD solver. Figure 5 shows the computational mesh zones and the overset mesh schematic illustration during computation. Since the DelFly uses a symmetric driving system, only one side of the wings is simulated. Hence, a symmetry plane is introduced at the position of the fuselage. As shown in Figure 5(a), there are four meshes in total, i.e. two sub-meshes for each wing, and two background meshes for smoothly transferring the mesh resolution. The global size of domain of the first and second layers of the background mesh are 16c×10c×14c and 6c×3c×5c, respectively. The domains of the wings are meshes with unstructured tetrahedrons, while the boundary layer is refined ($y_+ = 1$) with triangular-prisms. The background zones were meshed with a Cartesian grid (see Figure 5(b)). The cell amount for the each wing is around 1 million, and the total cell amount of the entire system is around 8 million. The simulation is first conducted to represent the hovering condition, i.e. without incoming freestream. The forward flight configuration will be further examined by introducing a coming freestream.

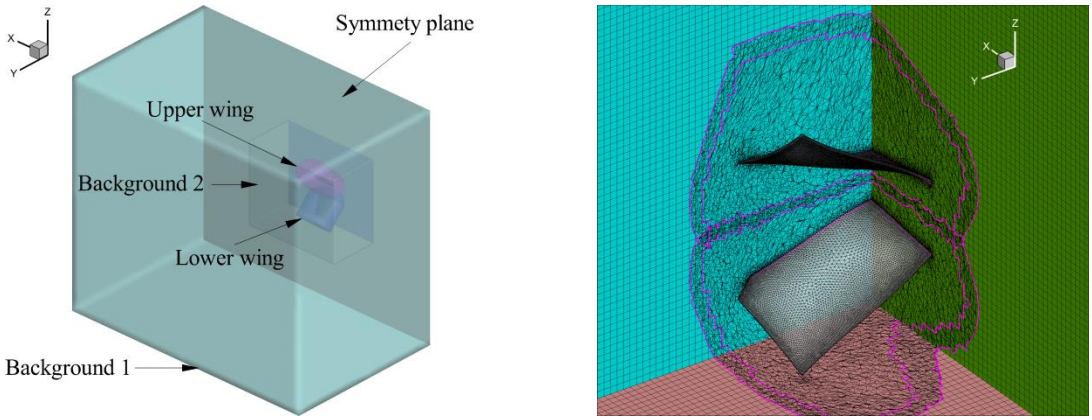

(a) (b)

Figure 5 Computational setup of the DelFly wings: (a) CFD mesh zones of the MAV wings; (b) overset mesh schematic show at t/T = 0.7, the purple solid lines shows the overset intergrid boundaries that used for data transfer.

III. Solver Verification and Validation

The verification assessment of the current CFD solver, i.e. convergence ability and order of accuracy has been presented in a previous study [13]. In this section, a validation will be carried out on the three-dimensional plunging wing experiments from Calderon et al. [23], and the aerodynamic force data and the flow fields are compared with the documented experimental results. The experiment was conducted on a rectangular wing with NACA0012 airfoil cross-section and a semi span aspect ratio of 2, with a freestream-based Reynolds number of 10,000. Forces and flow topology were captured via force balance and DPIV measurements, respectively. The case St = 0.45 (where St is the chord length based Strouhal number defined as $St = fc/U_\infty$) with an incident angle of 20 deg has been selected in our study for the purpose of validation. The computational domain is shown in Figure 6(a), the total number of cells for the wing and the background meshes is around 2 million, while the grid around the wing is refined at $y^+ = 1$. Figure 6(b) illustrates the overset scheme for a particular time instant. This simulation solves the fully laminar flow due to the relative low Reynolds number.

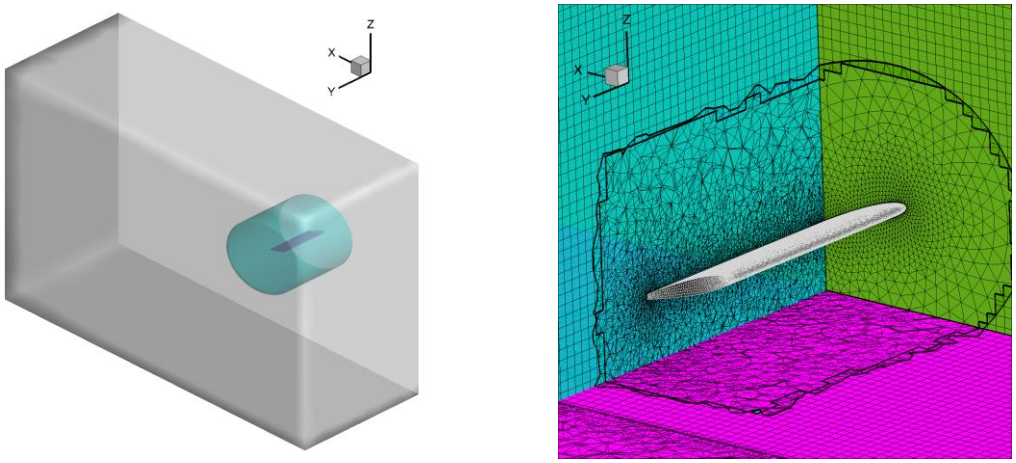

(a) (b)

Figure 6 Computational setup for the three-dimensional plunging wing: (a) computational domain; (b) overset grid at a certain time instant.

The comparison between the numerical and experimental results regarding time-average force coefficients is presented in Table 1, where it can be seen that the numerical simulation underestimates both the drag and lift coefficients, however, the values are still in a reasonable agreement (similar numerical results were also reported by Tay et al. [12]). The comparison of the flow field around the wing is depicted in Figure 7. The generation, translation and shedding of the leading and trailing edge vortices are clearly captured by the CFD solver, and the vortex pattern shows a good agreement with the PIV measurement.

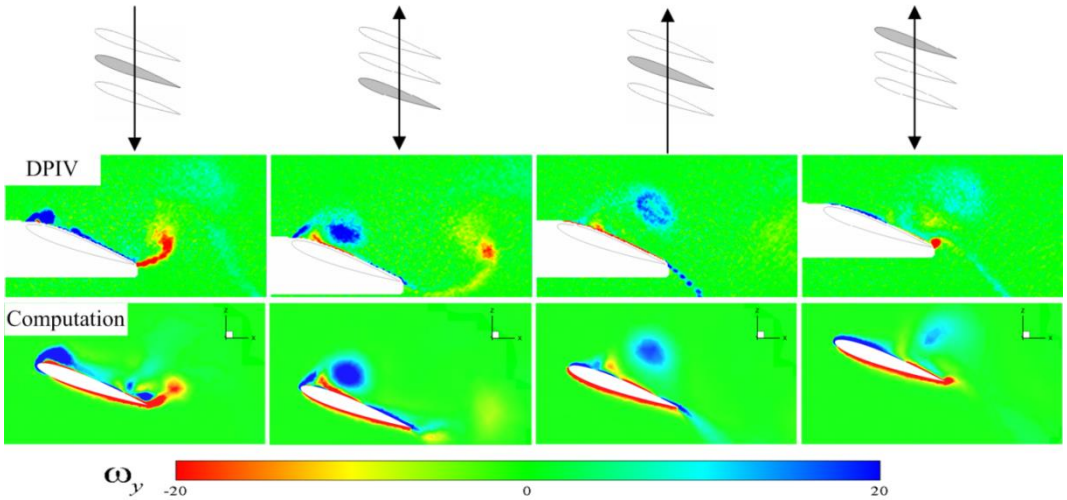

Figure 7 Flow topology comparisons between the DPIV and computational results, the DPIV snapshots were adapted from Calderon et al. [23].

Table 1 Force coefficients comparison between the experimental and numerical results

St_c	$\overline{C_d}$ (Calderon)	$\overline{C_d}$ (Comp)	$\overline{C_l}$ (Calderon)	$\overline{C_l}$ (Comp)
0.45	0.44	0.38 (-13.6 %)	1.36	1.28(-6 %)

IV. Results and Discussions

The resulting aerodynamic forces, as well as the flow topology including surface pressure distribution, velocity field and vortex structures are addressed and discussed in this section. The aerodynamic characteristics including the force generation and flow structures will be compared with the experimental results to evaluate the accuracy and feasibility of performing numerical simulations on the DelFly. It should be noted that the relevant force component under consideration is that in the X-direction (see Figure 1), and which in general is referred to as the thrust. However, since the measurement was performed with a horizontally oriented DelFly to represent the hover condition, the X-force in the current setup situation is identical to lift of the DelFly in hovering configuration.

A. Grid Convergence Study

It is important to investigate the convergence of the solution with increasing grid resolution and decresing time-step size. When the flow solver is discretized of the governing equation in a numerically consistent way for a laminar flow, the flow solution should converge to an asymptotical value with increasing spatial and temporal resolution. It is therefore a grid convergence study is performed for the DelFly in hovering configuration by varying the cell number of the sub-mesh, i.e., the grid system surrounds the flapping wings. Three grid systems were selected using different resolutions, i.e., around 0.5million, 1 million, and 2million. Note that, the experimental deformation was used to move the flapping wing meshes, i.e., 100 steps in constant, we thereby only test the spatial convergence accordingly.

Figure 8 plots the thrust coefficient variation during one flapping cycle for the aforementioned three different resolutions. As can be clearly seen the difference is occurred mostly around the peaks of the force profile where the flapping wings experiencing noticeable unsteady flow scenario, say during half instroke and outstroke.

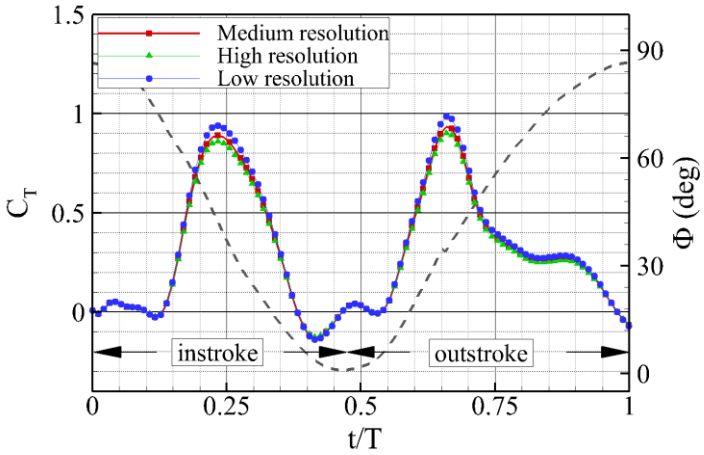

Figure 8 Thrust coefficients variation for different mesh resolution

The averaged thrust coefficients for the aforementioned three grid resolutions are shown in Table 2. It can be observed that the solution decreases asymptotically which should be the case. Moreover, the observed order of accuracy is around 2 which is normally consider a convincing grid resolution of choosing the medium mesh.

Table 2 Convergence test using Ct for one flapping period

Mesh Resolution	Low	Medium	High
$\overline{C_t}$	0.314	0. 301	0.296

B. Aerodynamic Characteristics in Hover

In Figure 9 the thrust coefficient variation during one flapping cycle is compared to the experimental data. The experimental thrust data was denoised by a zero-shift Chebyshev II low pass filter to get rid of the structural vibration effects. Based on the comparison between force measurements in vacuum and air conditions [16], the filtering cut-off frequency was determined so as to maintain the first three flapping harmonics, while the higher harmonics were considered as contributions from structural vibrations. The initial flapping wing position (t/T = 0.0) is defined as corresponding to the onset of the instroke, i.e. when the wings have reached their furthest distance and start moving towards each other again. In the numerical simulation, the clap and fling motion provides positive thrust over almost the entire cycle except for a short time interval during the transition phase (around t/T = 0.5). Two

thrust peaks are present, at around the middle of the instroke (t/T = 0.25) and the middle of the outstroke (t/T = 0.7), respectively, which can be attributed to the wings having the largest translation velocity at these instants. For the experimental result, the second peak (t/T = 0.7) has a noticeable larger amplitude than the first peak (t/T = 0.25) which is not existing in the numerical simulation, which can be clearly revealed from the Averaged thrust coefficient comparison in Table 3.

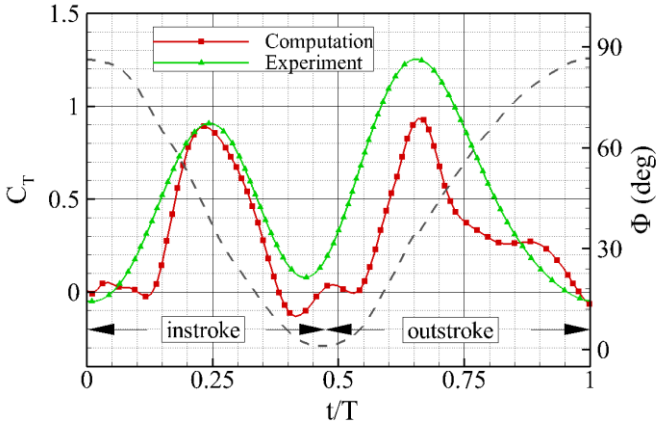

Figure 9 Thrust coefficients variation during one flapping cycle and its comparison with experimental data for the hovering configuration. Note that the black dashed line is the flapping phase angle (defined in Figure 1c) corresponds to the right vertical axis.

Table 3 Averaged thrust coefficient comparison between the experimental and numerical results

Clap (Instroke)		Fling (Outstroke)	
Exp	Num	Exp	Num
0.30	0.26	0.62	0.34

The instantaneous vortical structures and pressure contours at the corresponding time instants, approximately halfway during instroke (t/T = 0.25) and outstroke (t/T = 0.7), are plotted in Figure 10. A leading edge vortex (LEV), a trailing edge vortex (TEV) and a tip vortex (TV) structures for each wing are clearly observed. Note that root vortices are also created since the root part of the wings is cut off in the simulation, which is not the case in reality. Low pressure regions are formed on the outer surfaces (Figure 10(c)) during the instroke and on the inner surfaces (Figure 10 (d)) during the outstroke, which can be regarded as the primary source of the thrust generation.

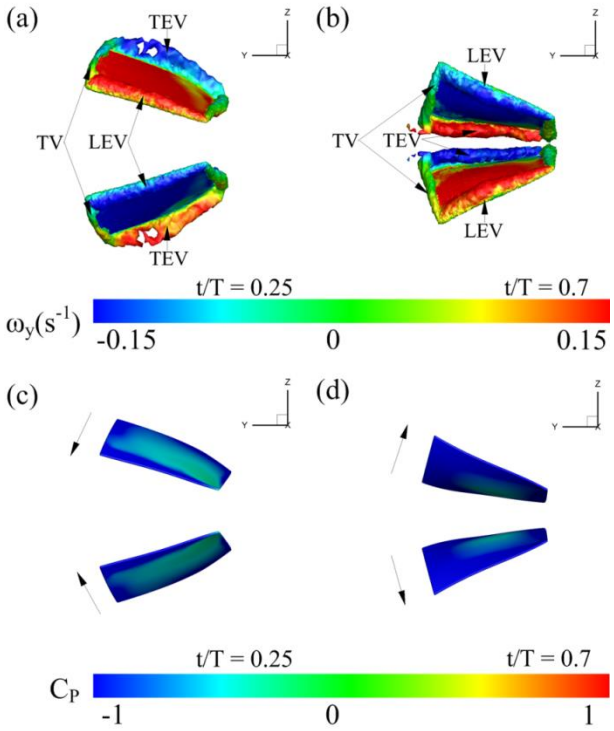

Figure 10 Instantaneous iso-surface of Q-criterion (Q = 100) and C_P contour during clap (t/T = 0.25) and fling (t/T = 0.7).

The computational force results show a similar tendency as the experimental force variation, and a good agreement is found in particular during the instroke phase. However, the computational result underestimates the thrust generation during the outstroke where the force peak was substantially higher in the experiment (by about 25%).

As documented, the clap and fling is regarded as an effective mechanism to strengthen the force production, where Ellington [24] conceived that for highly flexible wings the fling is more aptly described as peel. This concept expresses that the wings are curved along the chordwise direction (cf. Figure 4) and the point where the wings detach from each other moves smoothly from the leading to trailing edges during the early phase of the outstroke. Ellington [24] and Gotz [25] addressed that the aerodynamic effect of peel is more important than that of a rigid wing fling, in that the peel is substantially more effective in creating a circulation around the wings. In the experiment, the flexible wings of the DelFly displayed a peel event such that the trailing edge region remains impervious to the air flow for a substantial time during the onset of the fling phase. In contrast, in the numerical simulation a finite clearance (0.1c as can be seen in Figure 11(g)) between the wings is needed to be pre-defined in order to avoid the unwanted crossing of the walls and thus the trailing edges of the wings are not connected during fling. In the computation, therefore, this opening between the trailing edges allows the air to enter into the region

between the wings from all directions, which is likely to attenuate the force production via an inward momentum flux (see the flow field direction and the trailing edge vorticity in Figure 11(h)). The delayed build-up of the forces in the numerical simulations might be attributed to the formation of the trailing edge vortices as a result of this pre-defined clearance between the wings in view of the Wagner effect. However, in the actual flight of the DelFly, the formation of the trailing edge vortices is delayed due to the different behavior of the trailing edges such that they are rather attached to each other and start moving in the outstroke direction at a much later phase than the leading edges [16]. This result might explain the faster build-up of the forces in the measurements (Figure 8).

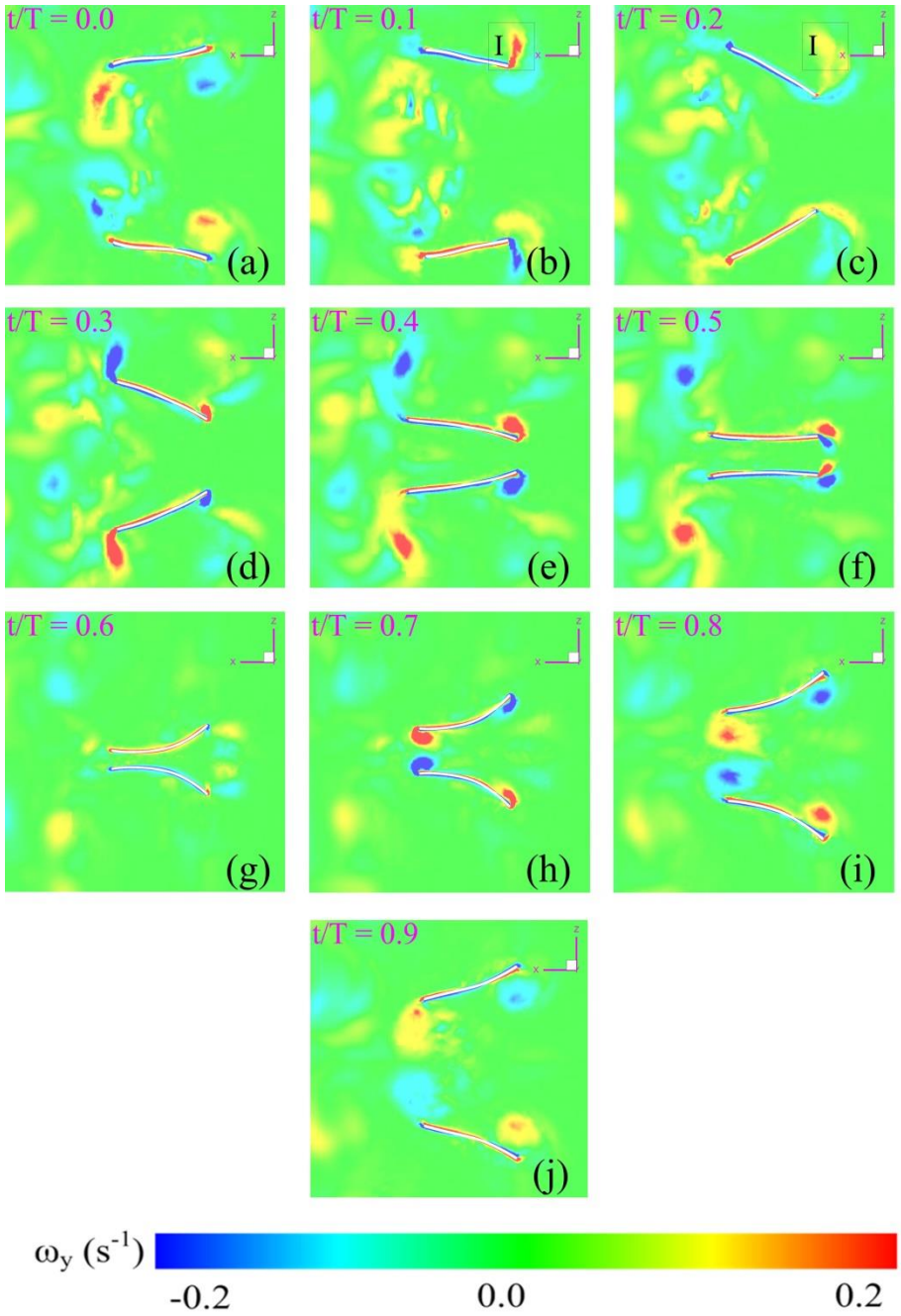

Figure 11 Vorticity contour during flapping at different time instants on a slice located at the 70% span length where can be regarded as representative of the aerodynamic performance. The flow vector (arrows) correspond to velocity vector at each point in the fluid, longer arrows signify larger velocities.

It is known that the LEVs can significantly enhance the force generation of a flapping wing. For the fling motion, the largest LEVs are generated around the time t/T = 0.7 where the thrust also peaks. However, looking at Figure 11, the strongest LEVs during instroke appear around t/T = 0.4, whereas the aerodynamic force peaks around t/T = 0.25 (see Figure 8). The most likely reason that maximum LEV strength and maximum thrust generation do not occur

simultaneously for the instroke, is that the LEV-induced forces work predominantly normal to the wing surface. At t/T = 0.4, the projected area along the x-direction is very small, such that the forces resulting from the LEVs have only a small component in that direction. Gotz [25] suggested that the force increase in clap is likely due to a jet of fluid squeezed out the closing gap between the trailing edge. In Figure 12, the mean fluid jet velocity during one flapping cycle is given, which was estimated by averaging the velocity profile in the gap between the wings at a streamwise position aligned with the trailing edges. A positive mean velocity indicative of a propulsive momentum contribution occurs during almost the complete instroke phase (t/T=0-0.5). The peak occurs at about t/T=0.3, yet there still exists a remarkable positive mean velocity during the clapping phase of the motion (t/T=0.45-0.5) even though the wings are rather stationary and parallel to each other in this period. In principle, the mean velocity at the monitoring position during the peel phase event should be zero since the trailing edge gap would be closed in the actual flapping conditions. However, because of the pre-defined clearance between the wings in the simulation and the associated formation of TEVs, there occurs a negative flow (directed toward the cleft between the wings), which can be considered as detrimental in terms of thrust force generation, as can be evidenced from Figure 9.

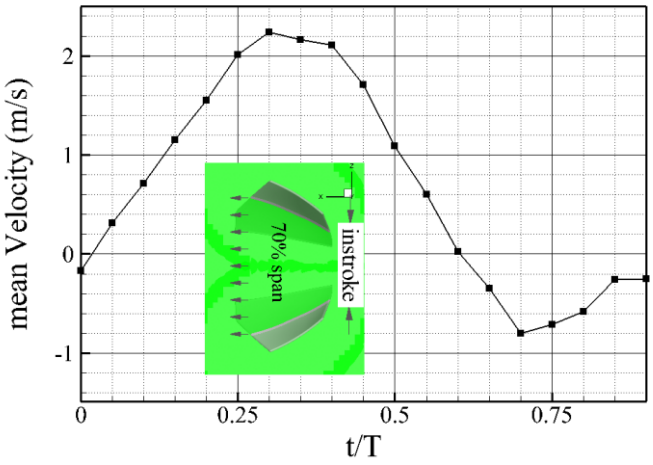

Figure 12 Temporal fluid jet flow associated with the clap event for the hovering configuration, the slice is oriented at 70% spanwise and the x-velocity was averaged only in the gap between the wings.

To gain an overall view of the three-dimensional flow structures of the DelFly in hovering configuration, the vortical structures at different time instants are visualized by means of the Q-criterion [26], which are rendered with y-vorticity for the sake of defining the rotational direction (seen in Figure 13). The plots illustrate very complex vortex structures, with the LEV, TEV and TV being the three dominant vortex structures which can be easily detected. At t/T = 0.0, when it is at the end of the outstroke, the LEV and the TV, that are generated during the

previous outstroke (LEV_{out} and TV_{out}, respectively), are observed to shed from the leading edge and tip. From t/T = 0.0 to 0.1, the wings are in the reversal flexing stage with the leading edges moving toward each other while the trailing edges are still moving apart. A vortical structure (see **I** in t/T = 0.1 in Figure 13) appears during this moment, such that it is formed by the rotating leading edge and it cannot stay attached to the wing surface due to the local high effective angle of attack. It is easier to clarify the formation and shedding of the vortical structure **I**, in Figure 11(b) and (c). As seen in t/T = 0.2 and 0.3, the vortical structure **I** will shed and diffuse. At the time of t/T = 0.3 during instroke, a new instroke LEV is generated on the outer surfaces of the wings and becomes larger at t/T = 0.4. These two contra-rotating LEVs are observed to become stronger (also see Figure 11(d) and (e)) until the wings move to the position of the onset of the outstroke. At this moment (Figure 13 (t/T = 0.5)) the wings are at their reversal stage (i.e. from instroke to outstroke), and an interaction of the wing and the instroke LEV formed during the instroke can be observed (see in Figure 11 (f)). The disturbed instroke LEV will shed and move forward (Figure 11(g)) and vanish eventually (t/T = 0.6). After that, during the outstroke motion, new LEVs are formed and developed (t/T = 0.7-0.9). Note that the shed TEVs and TVs travel very slowly into the wake, because in hovering configuration the convection velocity is entirely self-induced.

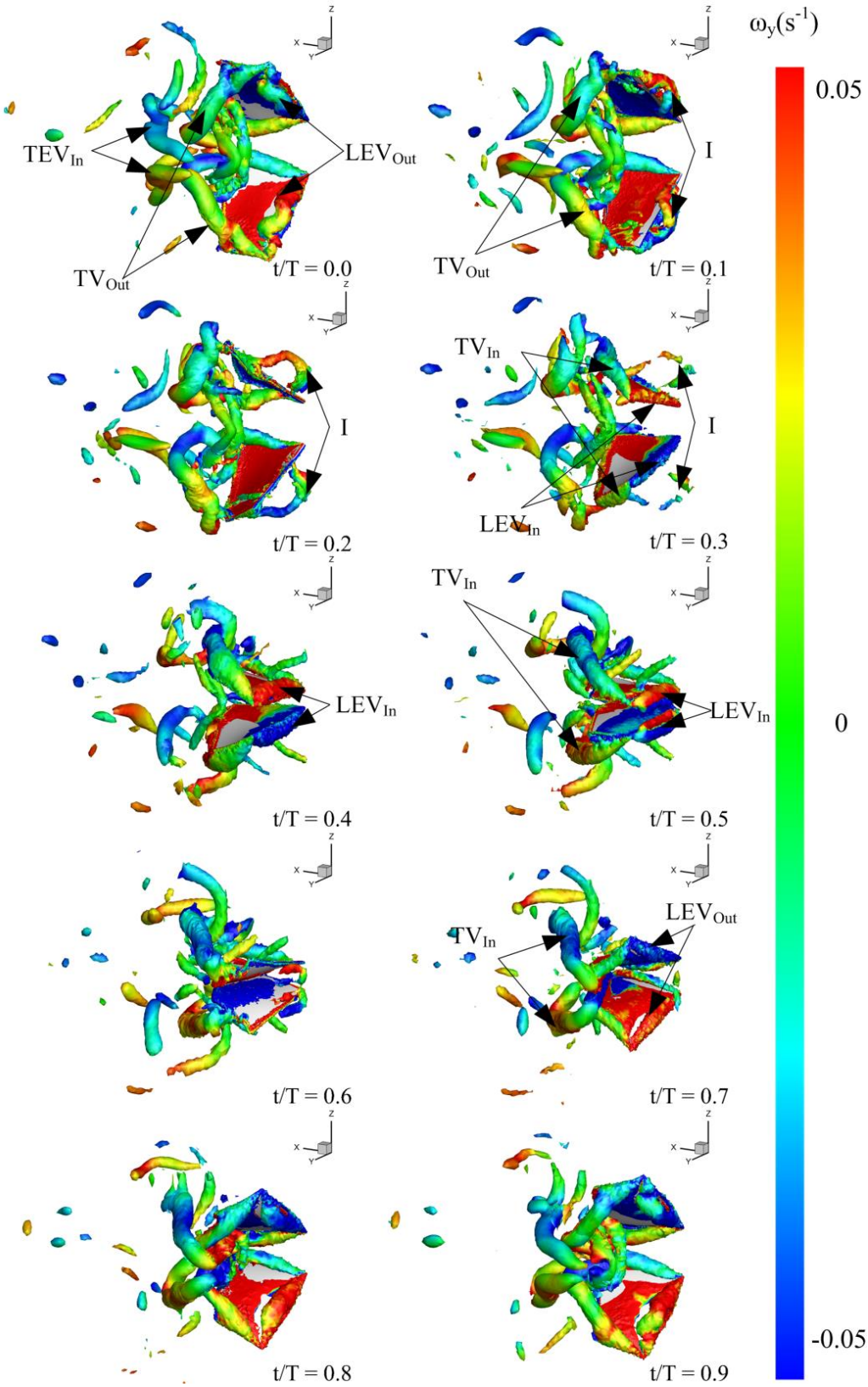

Figure 13 Isosurface of Q-criterion (Q = 100) colored with y-vorticity in hover during one flapping cycle.

C. Force enhancement by clap and fling

The clap and fling mechanism is employed on the DelFly flapping-wing MAV in view of its alleged considerable force enhancement effect as also documented abundantly in literature. In this section it is attempted to estimate the actual benefit of the DelFly by this mechanism. In order to do so, simulations were performed with only the top wing present, so as to eliminate the wing to wing interaction due to the clap and fling. The numerical meshes and the wing deformation for the single-wing simulation are kept the same as for the original two-wing simulation which exhibits the clap and fling effect. Although in reality the fluid-structure interaction and, hence, the deformation characteristics of a single wing would be different from that of the double wing, the current approach allows to study the fluid-dynamic effect in isolation. The thrust generation for the two geometries, i.e. single wing and double wing, is shown in Figure 14. It is clear that the double-wing flapping configuration generates more aerodynamic force than the sing-wing flapping case. The time-averaged thrust coefficients are 0.3 and 0.25 for the double and single wing cases, respectively. The thrust generation is nearly identical during the instroke phase, whereas the force generation is remarkably enhanced during the outstroke phase, which can be attributed to the clap-and-peel motion occurring during the stroke reversal.

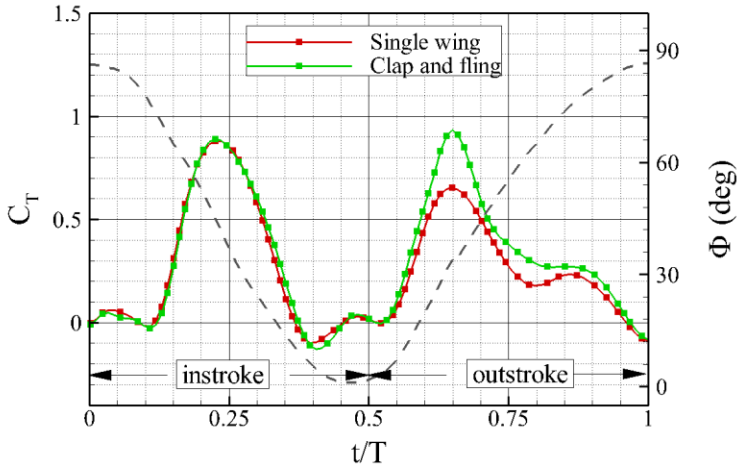

Figure 14 Thrust coefficients enhancement by the clap and fling mechanism in hovering configuration.

The thrust is enhanced by 42% in the peak region at around t/T = 0.66. As mentioned by Sane [27], the approaching two wings at the end of instroke will tend to annul the opposing circulations of each other. As a result, the shed trailing edge vorticity will be considerably attenuated or absent, allowing the wings to build up circulation more rapidly and thus to produce more lift over time in the subsequent stroke (reduced Wagner effect). The

corresponding event at t/T = 0.7 is visualized in Figure 15, where the spanwise section at 70% span. Due to the introduction of the lower wing, a low pressure region is created between the wings as seen in Figure 15(a). This promotes the air flow around the leading edges (as seen in Figure 15(b)), which results in larger LEVs peak compared to the single wing case (see Figure 15(c)). This effect of fling has been experimentally verified by Lehmann et al. [28] using PIV measurements.

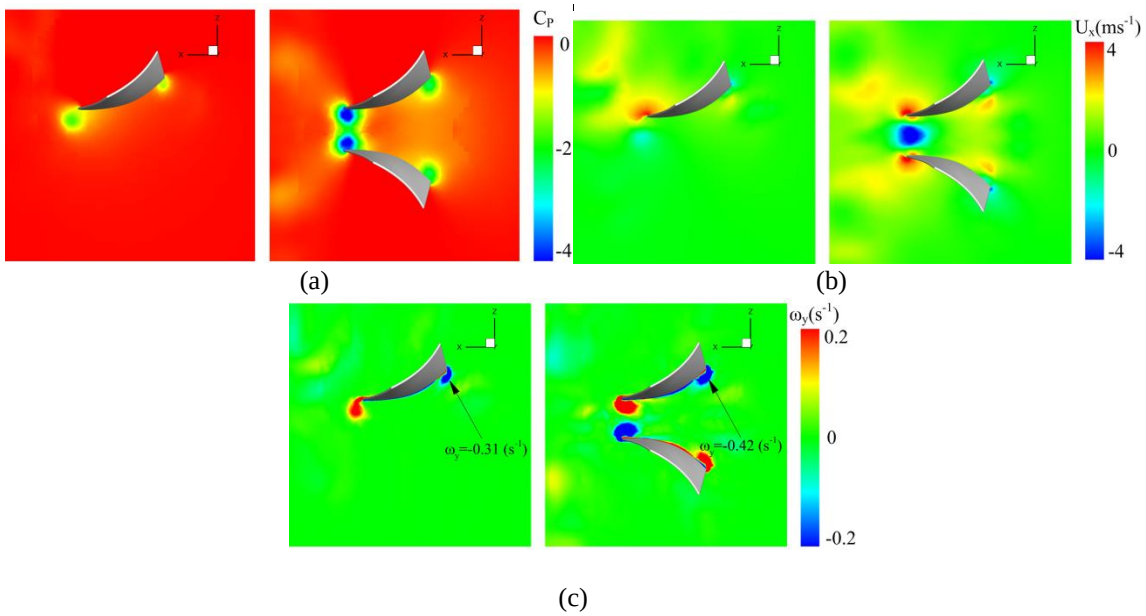

Figure 15 Flow field comparison between the single and clap-and-fling configurations at t/T = 0.7: (a) pressure; (b) x-velocity; (c) y-vorticity; the slice is located at the 70% chord.

Considering the clap phase, on the other hand, Ellington [3] addressed that the fluid ejected from the closing gap at the end of the clap will produce a rearward momentum jet that augments thrust force generation. Numerical simulations on both two-dimensional [29] and three-dimensional [30] flapping wings across a range of Reynolds numbers supported this suggestion that the clap is likely to enhance lift production to some extent. However, such a scenario does not appear to occur during the clap event of the DelFly MAV as seen at the end of instroke in the force history (Figure 14), where no appreciable difference is observed between the single-wing and double-wing configurations. One possible explanation is that towards the end of the instroke the wings will be more or less parallel to each other, so that the wing to wing interaction will not be effective in enhancing the force component in the thrust direction. On the other hand, at the onset of the instroke, the distance between the wings is large, such that there is little interaction. The wings are more or less working individually, thus there is no force enhancement from the wing to wing interaction during instroke.

D. Effect of Freestream Velocity

The flow structure for the hovering condition, as depicted in Figure 13, is quite complex due to the absence of a freestream flow that would convect the generated vortical structures away from the wings. In this section, simulations will be conducted for forward flight conditions, defined by introducing a freestream velocity, at 1, 2 and 3 m/s. Generated flow structures will be visualized to evaluate the effect of incoming freestream and compared to experimental PIV results from [8]. Note that for these simulations the wing deformation data that was acquired in the hovering configuration was used, under the assumption that these are not significantly altered by the addition of a freestream velocity. The flow structure for the case with a freestream velocity U_∞ = 1 m/s is shown in Figure 16 at four different moments during the flapping cycle. The vortex structures generated during the instroke and outstroke phases are clearly visualized and indicated by the boxes labelled as **I** and **O**, respectively. Comparing with the hover configuration in Figure 13, the flow structures under the effect of the freestream flow are seen to be convected faster downstream, as expected. The TV shed during outstroke (b in Figure 16) is connected with the vortex shed from the previous instroke (**I** in Figure 16). A new vortex ring is generated and shed from each flapping wing during instroke, seeing **I_1** and **I_2** in Figure 16. Note that the vortex structure on the root part is likely to be substantially different from that of the real DelFly flapping-wing MAV, in view of the wing root cut-out used in the simulations (see section II.B), still the alternatively shed instroke and outstroke structures provide a good agreement with the experimental results from PIV measurements, as discussed below.

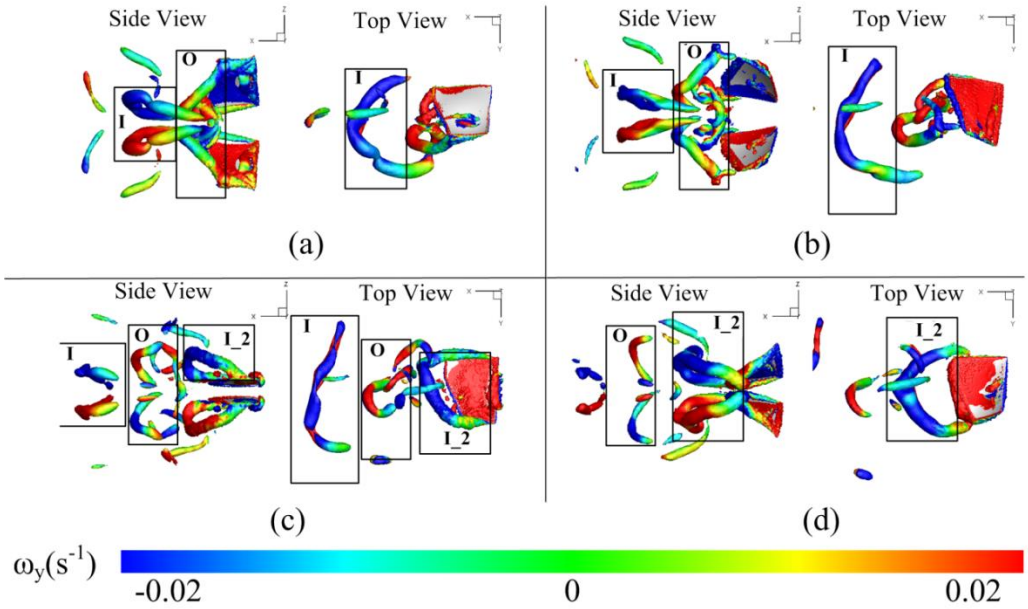

Figure 16 Flow structures with incoming freestream U_∞ = 1 m/s at different time instants, the iso-surface plot is Q = 100 colored by the y-vorticity: (a) t/T = 0.00; (b) t/T = 0.25; (c) t/T = 0.50; (d) t/T = 0.75.

Figure 17 shows the flow structure of the DelFly flapping wings with different freestream velocities of 1, 2 and 3 m/s at time instant, t/T = 0.25. The velocity value does not introduce a significant change in the structure topology, in that the dominated structures during instroke and outstroke appear quite similar in shape. A higher velocity will result in a longer wavelength of the wake, as the structures are more quickly transported downstream relative to the flapping period. Therefore, the instroke and outstroke structures are quite isolated at higher freestream velocity.

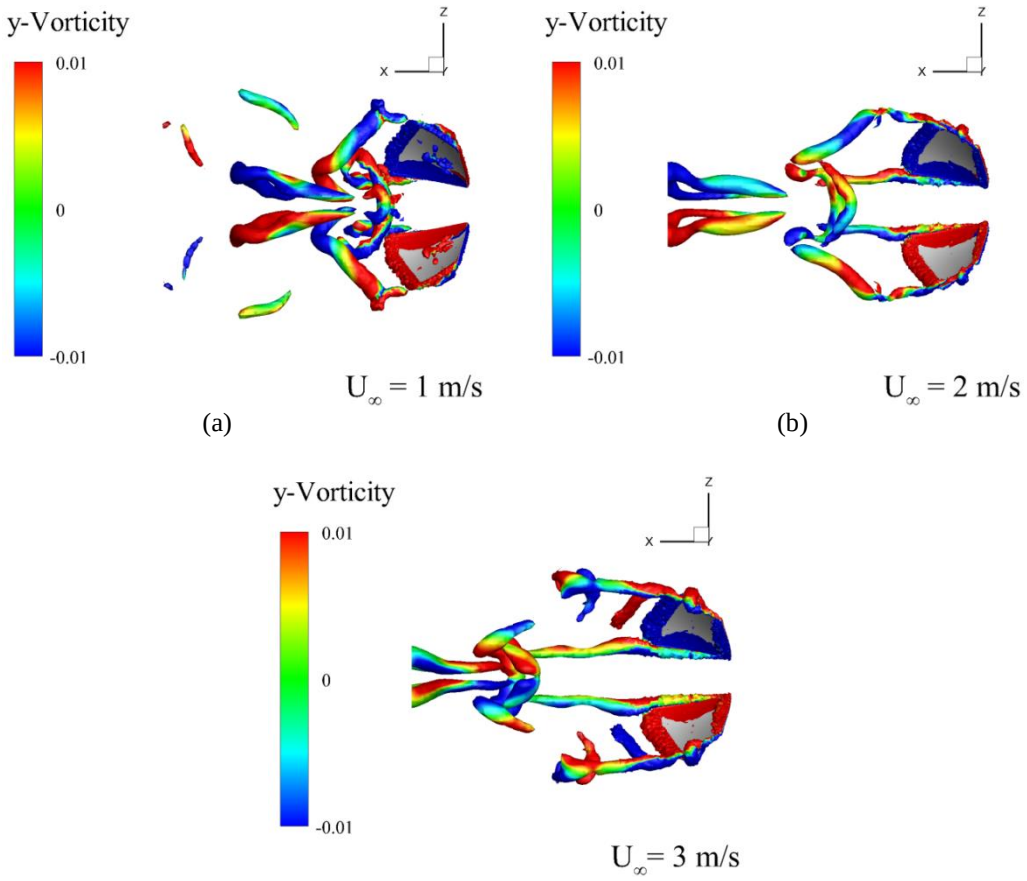

Figure 17 Flow structures with varying incoming freestreams at t/T = 0.25; the iso-surface plot is Q = 100 colored by the y-vorticity: (a) t/T = 0.00; (b) t/T = 0.25; (c) t/T = 0.50; (d) t/T = 0.75.

Figure 18 shows the comparison between the numerical and the experimental results reported by Percin et al. [8] in terms of the three-dimensional vortical structure in the wake, for similar values of the reduced frequency. The latter is defined as $k=\pi fc/U_\infty$, where f is the flapping frequency, c the mean wing chord (80 mm) and U_∞ the freestream velocity. In the experimental study, stereoscopic PIV was used to measure the wake flow and the three-dimensional wake structures were subsequently reconstructed using the temporal flow information of one stationary measurement plane, using an advection model based on Taylor's hypothesis. Note that this approach assumes that

the vortical structures do not deform when traveling downstream and also because no information in the direct vicinity of the wings is available. Particularly for the structures generated during outstroke there is a good agreement between numerical simulation and experiments, see number 3 and 4 in Figure 18. Moreover, the vortex-vortex interaction between the upper and lower wing structures (see number 5 in Figure 18) is captured in the higher reduced frequency case and is not visible at the lower reduced frequency case. However, the instroke structures (1 and 2 in Figure 18) are closer to each other in the simulation where a disparity exists with respect to the experiments. These differences can possibly arise from differences in the setup of the numerical simulation and the experiment, such as: (1) The deformation is measured during the hovering configuration and is not exactly the same in the forward flight situation; (2) The wing thickness is different (5 μm Mylar foil in experiment, 2 % chord in the computation); (3) The root part in the numerical simulation was omitted during the computation for the sake of simplification; (4) A small clearance between the upper and lower wings needed to be applied in the numerical simulations, which influences the pressure distribution and flow behavior between the wings, especially in the fling phase.

These considerations suggest that the wing kinematic and deformation patterns can significantly influence the flow structure, implying that a proper wing characterization is required for an accurate prediction of the flow structure around the flexible flapping wings. However, it has been shown that notwithstanding the deficiencies in the current modeling of the wing behavior, the numerical simulation in the present study is able to capture the dominant flow structures during outstroke and instroke with a good extent of agreement with the experimental findings, such that is results can provide a general insight of the flapping wing aerodynamics.

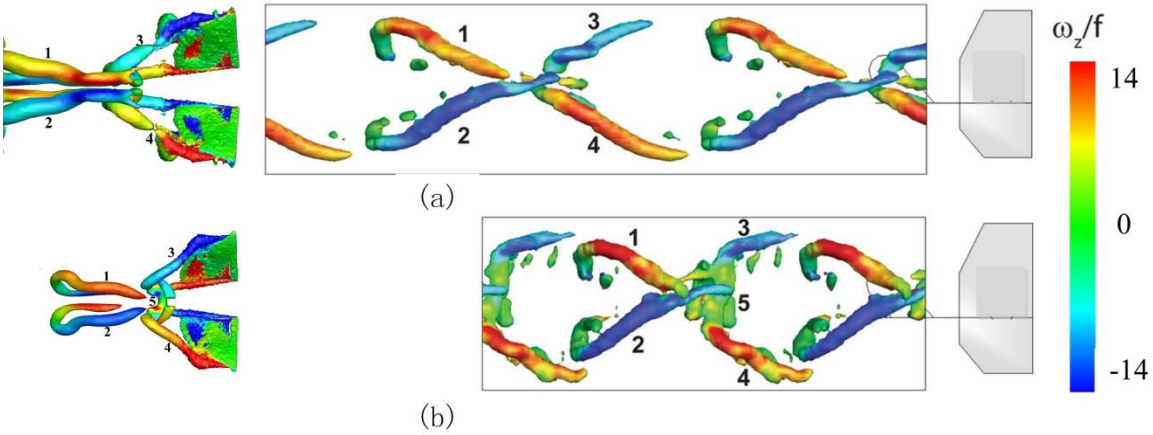

Figure 18 Side view of the comparison between the numerical (left) and experimental (right) results at two different values of the reduced frequency, the iso-surface plot is Q = 100 colored by the ω/f: (a) U_∞ = 3 m/s; k = 0.67; (b) U_∞ = 2 m/s k = 1.00. (The experimental snapshots are adapted from Percin et al. [8])

V. Conclusion

The aerodynamic characteristics of a flapping-wing MAV, the DelFly were numerically simulated using an in-house developed CFD solver. The code solves the unsteady compressible Navier-Stroke equations with a low Mach preconditioning. To accurately model the kinematics of the DelFly flapping wings, the morphological deformation pattern derived from a stereo-vision experiment was used as a prescribed input to the solver, thus omitting the need for a complex fluid-structure interaction model. As the flapping wings experience large relative motions, a deformable overset dynamic mesh method is employed to dynamically implement the instantaneous mesh system.

The formation and evolution of the vortical structures (LEV, TEV and TV) are clearly visualized by the simulations. In the hover configuration, the vortical structures are advected only by self-induction, and hence tend to remain near the wing, resulting in a complex pattern with mutual interactions. The flow structures were put in connection to the force production, providing explanation for the force generation mechanisms. In addition, the numerical force results were compared with experiments, in which the force was measured by a miniature force sensor. Overall speaking, the trend of the force variation was similar for experiment and numerical simulation. A very good agreement is revealed for the instroke phase in particular, while a significant underestimation with respect to the experiment occurs in the outstroke. The latter disparity is attributed to the effect of a minimum clearance between the wings that needed to be applied in the simulations.

The force enhancement by the clap and fling mechanism was further investigated by comparing the results from a single flapping wing simulation, in which this interaction effect is absent. The beneficial effect of the fling phase was indeed confirmed, with stronger LEVs generated during outstroke. The clap mechanism in the numerical simulation, on the other hand, was not found beneficial to the force enhancement because the wings are more or less parallel to each other at the end of outstroke, thus neutralizing the interaction.

The effect of freestream velocity on the aerodynamic performance of DelFly (which can be regarded as representing the forward flight configuration) was addressed by introducing a wind speed at 1, 2 or 3 m/s. We found that the vortex structures are qualitatively similar for different velocities and mainly change in wavelength, i.e. a larger incoming velocity will stretch the wake to a larger extent. By comparing the flow structure with experimental results, the dominant flow structures are found to be reliably captured and a similar behavior was revealed. These

results show that the computational procedure provides a quantitative prediction of the unsteady aerodynamics of the flapping-wing MAV in terms of aerodynamic force production and flow structures.

Acknowledgments

This work has been supported by the Netherlands Technology Foundation (STW, project number 11023) and the National Science Foundation of China (No. 11002072). The support from China Scholarship Council (CSC, No. 2011683005, No. 201303070173) is also appreciated. The authors also want to thank Dr. Jouke de Baar for his assistance in the Kriging regression of the data.

References

[1] Mueller, T.J., "Fixed and Flapping Wing Aerodynamics for Micro Air Vehicle Application (Progress in Aeronautics and Astronautics)," Reston, VA: *AIAA*, 2001.

[2] Weis-Fogh, T., "Quick Estimates of Flight Fitness in Hovering Animals, Including Novel Mechanisms for Lift Production," *Journal of Experimental Biology*, Vol. 59, pp. 169-230, 1973.

[3] Ellington, C.P., Van De Berg, C., and Willmott, A.P., "Leading-Edge Vortices in Insect Flight," *Nature*, Vol. 384, pp. 626-630, 1996.

[4] Dickinson, M.H., "The Effects of Wing Rotation on Unsteady Aerodynamic Performance at Low Reynolds Numbers," *Journal of Experimental Biology*, Vol. 192, pp.179-206, 1994.

[5] Pornsin-Sirirak, T.N., Tai, Y.C., Ho, C.M., and Keennon, M., "Microbat: A Palm-sized Electrically Powered Ornithopter," *NASA/JPL Workshop on Biomorphic Robotics*, August 14-17, 2001, Pasadena, CA.

[6] Gafford, J.B., Kesner, S.B., Wood, R.J., and Walsh, C.J., "Microsurgical Devices by Pop-up Book MEMS," *Proceedings of the ASME 2013 International Design Engineering Technical Conferences & Computers and Information in Engineering Conference*, August 4-7, 2013, Portland, Oregon, USA.

[7] De Croon, G.C.H.E., De Clercq, K.M.E., Ruijsink, R., Remes, B., and De Wagter, C., "Design, Aerodynamics and Vision-based Control of the DelFly," *Bioinspiration and Biomimetics*, Vol. 1, No 2, pp. 71-97, 2009.

[8] Percin, M., van Oudheusden, B.W., Eisma, H.E., and Remes, B.D.W., "Three-dimensional Vortex Wake Structure of a Flapping-wing Micro Aerial Vehicle in Forward Flight Configuration," *Experiments in Fluids*, Vol. 55, No. 1806, 2014.

[9] Tenaglia, A., Percin, M., van Oudheusden, B.W, Deng, S., and Remes, B., "Vortex Formation and Force Generation Mechanisms of the DelFly II in Hovering Flight," *International Micro Air Vehicle Conference and Competition*, 2014, August 12-15, Delft, the Netherlands.

[10] Gillebaart, T., Tay, W.B, van Zuijlen, A.H., and H. Bijl., "A Modified ALE Method for Fluid Flows Around Bodies Moving in Close Proximity ", *Computers and Structures*, Vol. 145, pp. 1-11, 2014.

[11] De Clercq, K.M.E., De Kat, R., Remes, B., van Oudheusden, B.W., and Bijl, H., "Flow Visualization and Force Measurements on a Hovering Flapping-wing MAV DelFly II," *39th AIAA Fluid Dynamics Conference*, 22-25 June 2009, San Antonio, USA, AIAA-2009-4035.

[12] Tay, W.B., van Oudheusden, B.W., and Bijl, H., "Numerical Simulation of a Flapping Four-wing Micro-Aerial Vehicle," *Journal of Fluids and Structures*, Vol. 55, pp. 237-261, 2015.

[13] Deng, S., Xiao, T., Percin, M., van Oudheusden, B.W., Bijl, H., and Remes, B., "Numerical Simulation of DelFly Flapping Wing MAV by means of a Deforming Overset Grid Method," *22nd AIAA Computational Fluid Dynamics Conference*, 22-26, June, Dallas, USA, AIAA-2015-2615.

[14] Bruggeman, B., "Improving Flight Performance of DelFly II in Hover by Improving Wing Design and Driving Mechanism," *Master Thesis*, Delft University of Technology, 2010.

[15] Groen, M., Bruggeman, B., Remes, B., Ruijsink, R., van Oudheusden, B.W., and Bijl, H., "Improving Flight Performance of the Flapping wing MAV DelFly II", *IMAV Conference*, Braunschweig, Germany, 2010.

[16] Percin, M., "Aerodynamic Mechanisms of Flapping Flight," *Doctoral Thesis*, Delft University of Technology, 2015.

[17] De Baar, J.H.S., Percin, M., Dwight, R.P., van Oudheusden, B.W. and Bijl, H., "Kriging Regression of PIV Data Using a Local Error Estimate," *Experiments in Fluids*, Vol. 55, No. 1650, 2014.

[18] Chorin, A.J., "A Numerical Method for Solving Incompressible Viscous Flow Problems," *Journal of Computational Physics*, Vol. 135, No. 2, pp. 118-125, 1997.

[19] Turkel, E., "Preconditioned Methods for Solving the Incompressible and Low Speed Compressible Equations," *Journal of Computational Physics*, Vol. 72, No. 2, pp. 277-298, 1987.

[20] Choi, Y.H., and Merkle, C.L., "The Application of Preconditioning to Viscous Flows," *Journal of Computational Physics*, Vol. 105, No. 2, pp. 207-223, 1993.

[21] Saad, Y. "A Flexible Inner-Outer Preconditioned GMRES Minimal Algorithm," Siam Journal on Scientific

Computing, Vol. 12, No. 2, pp. 461-469, 2006.

[22] Zhang, L.P., and Wang, Z.J. "A Block LU-SGS Implicit Dual Time-stepping Algorithm for Hybrid Dynamic Meshes." Computers and Fluids, Vol. 33, No. 7, pp. 891-916, 2004.

[23] Calderon, D.E., Wang, Z., and Gursul, I., "Lift Enhancement Vortex Flows Generated by Plunging Rectangular Wings with Small Amplitude". AIAA Journal, Vol. 51, No. 12, pp. 2953-2964, 2013.

[24] Ellington, C.P., "The Aerodynamics of Hovering Insect Flight. IV. Aerodynamic Mechanisms," *Phil. Trans. R. Soc. Lond. Series B*, Vol. 305, pp. 79-113, 1984.

[25] Gotz, K.G., "Course-Control, Metabolism and Wing Interference during Ultra long Tethered Flight in Drosophila Melanogaster," *Journal of Experiment Biology*, Vol. 128, pp. 35-46, 1987.

[26] Hunt, J.C.R., Wray, A.A., and Moin, P., "Eddies, Streams, and Convergence Zones in Turbulent Flows," Proceedings of the summer program, Center for turbulence research, pp. 193-208, 1988.

[27] Sane, S.P., "The Aerodynamics of Insect Flight," *Journal of Experimental Biology*, Vol 206, pp. 4191-4208, 2003.

[28] Lehmann, F.O., Sane, S.P., and Dickinson, M., "The Aerodynamic Effects of Wing-wing Interaction in Flapping Insect Wings," *Journal of Experimental Biology*, Vol. 208, pp. 3075-3092, 2005.

[29] Sun, M., and Yu, X., "Flow Around Two Airfoils Performing Fling and Subsequent Translation and Translation and Subsequent Clap," *Acta Mechanica Sinica*, Vol. 19, No. 2, pp. 103-117, 2003.

[30] Miller, L.A and Peskin, C.S., "When Vortices Stick: An Aerodynamic Transition in Tiny Insect Flight," *Journal of Experimental Biology*, Vol. 207, pp. 3073-3088, 2004.